Fin field-effect-transistor engineered sensor for detection of MDA-MB-231 breast cancer cells: A switching-ratio-based sensitivity analysis

Bhavya Kumar [*] and Rishu Chaujar [†]

Department of Applied Physics, Delhi Technological University, Delhi 110042, India

The present study describes the utilization of a gallium-arsenide gate-stack gate-all-around (GaAs-GS-GAA) fin field-effect transistor (FinFET) to accomplish the electrical identification of the breast cancer cell MDA-MB-231 by monitoring the device switching ratio. The proposed sensor uses four nanocavities carved beneath the gate electrodes for enhanced detection sensitivity. MDA-MB-231 (cancerous) and MCF-10A (healthy) breast cells have a distinct dielectric constant, and it changes when exposed to microwave frequencies spanning across 200 MHz and 13.6 GHz, which modifies the electrical characteristics, allowing for early diagnosis. First, a percentage shift in the primary DC characteristics is presented to demonstrate the advantage of GS-GAA FinFET over conventional FinFET. The sensor measures the switching-ratio-based sensitivity, which comes out to be 99.72% for MDA-MB-231 and 47.78% for MCF-10A. The sensor was tested for stability and reproducibility and found to be repeatable and sufficiently stable with settling times of 55.51, 60.80, and 71.58 ps for MDA-MB-231 cells, MCF-10A cells, and air, respectively. It can distinguish between viable and nonviable cells based on electrical response alterations. The possibility of early detection of cancerous breast cells using Bruggeman's model is also discussed. Further, the impact of biomolecule occupancy and frequency variations on the device sensitivity is carried out. This study also explains how to maximize the sensing performance by adjusting the fin height, fin width, work function, channel doping, temperature, and drain voltage. Lastly, this article compared the proposed breast cancer cell detectors to existing literature to evaluate their performance and found considerable improvement. The findings of this research have the potential to establish GaAs-GS-GAA FinFET as a promising contender for MDA-MB-231 breast cancer cell detection.

I. INTRODUCTION

Cancer is not an infectious illness; instead, it is caused by a malfunction in the DNA of a cell or tissue [1]. These cells do not perform their usual functions but rather proliferate and replicate in an uncontrolled manner, resulting in the formation of a tumor. In 2020, according to WHO fact sheets, cancer was the leading cause of mortality worldwide, accounting for around 10 million deaths, or almost one in every six, with breast cancer (2.26 million cases) as the most prevalent cancer, followed by lung cancer (2.21 million cases), colon and rectum cancer (1.93 million cases), and so on [2]. The formation of malignant tumors in women's breasts is the primary cause of breast cancer, and the lifetime chance of developing it is 12%. The most common cancerous breast cells are MDA-MB-231, MCF-7, T47D, and Hs578t, while MCF-10A is a healthy nontumorigenic breast cell [1]. Compared to MCF-7 and T47D, Hs578t and MDA-MB-231 cells are regarded as the most invasive. Since invasive breast cancer cells are so dangerous and may spread rapidly, diagnosis at an early stage is very important. Early diagnosis may aid in more effective disease management, and more than 70% of cases are expected to be cured with early detection [3,4].

Cell isolation separates one or more particular cell populations from a heterogeneous mixture of cells. Targeted cells are identified, isolated, and then segregated by kind. Many cell isolation techniques are available depending on the kind of cells being separated, with a few significant ones covered in this paper, each having pros and cons. The computer-controlled micropipette (CCMP) method uses a small glass or quartz micropipette with a fine tip that a computer can control to precisely separate cells. CCMP involves manipulating a micropipette towards a suspended cell and applying a tiny suction pressure to partly aspirate the cell within the micropipette. As suction pressure rises, the cell deforms and flows into the micropipette. Researchers have widely employed this approach to explore the adhesion force measurements [5] and mechanical characteristics of diverse cells [6,7]. Fluorescence-activated cell sorting (FACS) is a flow cytometry method that uses fluorescence characteristics to separate cells. FACS begins with labeling cells with fluorescent dyes that attach to specific cell surface markers. In front of a laser, the suspended cells are passed in a stream of droplets, each containing a single cell. This stream is then directed via a series of lasers, which activate the cell-bound fluorophores, resulting in light scattering and fluorescent emissions. The fluorescence detecting system recognizes cells of interest based on the wavelengths generated by the laser excitation. Due to its wide application, FACS research includes bacteria [8], protoplasts [9], bone marrow

*bhavyakumar_phd2k18@dtu.ac.in
†chaujar.rishu@dtu.ac.in

cells [10], etc. Microfluidics is a cell separation technique that uses fluid manipulation on a microscopic scale. Cell isolation approaches based on microfluidics vary depending on their size, density, compressibility, electrical and magnetic characteristics, etc. The membrane filtering technique uses thin membrane layers with micropores to detect and isolate cells based on their size [11]. Cells of different densities and compressibilities may be separated using acoustic waves in a process called acoustophoresis [12]. In dielectrophoresis, nonuniform electric fields separate and isolate cells based on their dielectric properties [13]. Cells that contain magnetic nanoparticles may be identified and separated via magnetic cell sorting [14]. Laser microdissection is a high-resolution technique for isolating cells from their surrounding tissues that employs a laser beam and direct microscopic visualization. The sample is mounted on a microscope slide, and an infrared or ultraviolet laser selectively cuts off the cells of interest. After that, the sliced cells are collected for further examination. This technique has been extensively used in the research of liver illnesses [15], mass spectrometry [16], etc.

X-ray mammography, sonography, and magnetic resonance imaging (MRI) scans are some screening methods for breast cancer identification. Currently, x-ray mammography is the predominant method for breast cancer detection. Although this technology has made significant strides in this sector, there have been reports of many drawbacks [17,18]. In addition, x-ray mammography's specificity and sensitivity drastically decrease to 89% and 67% for dense breasts, and the method also includes radiation exposure dangers [19]. While sonography may be a cost-effective tool in the fight against breast cancer, the accuracy of a diagnosis relies on the experience of the person doing the procedure, and hence it may provide erroneous findings at times [20]. MRIs with improved contrast have a higher sensitivity (93–100%) [21], but they are difficult to use, costly, and limited to hospital use.

The microwave imaging technique was created to overcome the drawbacks of conventional imaging. This method uses the large dielectric difference between healthy and cancerous tissue to perform microwave imaging and heating [22–24]. Scientists have been interested in how different types of malignant cells behave and may be detected when exposed to microwave frequencies [25,26]. Kim *et al.* calculated the dielectric characteristics of fatty glandular, fibro, and malignant breast tissues from 50 MHz to 5 GHz frequency [27]. It was noted that the dispersion of malignant tissues differs from that of healthy breast tissue. In the frequency range of 50–900 MHz, Joines *et al.* investigated the dielectric characteristics of human tissues and found that cancerous tissues have greater conductivity and permittivity than normal tissues [28]. Many investigations have been conducted to know the dielectric characteristics of various human body components, such as the liver [29]. Dielectric characteristics of numerous *in vitro* breast malignant cell lines have been examined between 200 MHz and 13.6 GHz by Hussein *et al.* [1]. It was found that breast cancer cells, because of their high water content, exhibit varying dielectric characteristics, leading to enhanced scattering at microwave frequencies.

Compared to imaging methods, molecular biotechnology tests may detect breast cancer sooner. However, they cannot substitute imaging techniques but complement imaging methods for diagnosing breast cancer. Molecular biotechnology examines biomarkers like nucleic acid, proteins, cells, and tissues of patients. Effective molecular biotechnology examination tools utilized for identifying breast cancer cells include quantitative polymerase chain reaction (qPCR), mass spectrometry (MS), single-cell resonant waveguide gratings (SCRWGs), digital holographic microscopy (DHM), etc. The qPCR, or real-time PCR, quantifies DNA and gene expression levels in samples. qPCR has been used to assess circulating tumor cells in many solid tumors, such as breast cancer [30]. The qPCR technology may guide breast cancer therapy by monitoring mRNA expression [31]. Matrix-assisted laser desorption/ionization (MALDI) mass spectrometry imaging (MSI) [32], surface-enhanced laser desorption/ionization (SELDI) MS [33], and liquid chromatography-tandem mass spectrometry (LC-MS/MS) [34] are some of the MS-based techniques utilized for breast cancer diagnosis. The concentration of adhesion proteins inside the cell-substrate contact zone causes a change in the refractive index, which may be monitored in real-time using SCRWGs. The SCRWGs technology was used to monitor the adhesion of HeLa cancer cells [35]. DHM technology provides high-resolution three-dimensional (3D) imaging of transparent biological specimens such as live cells and tissues. DHM may be utilized to capture digital holograms of breast tissues and analyze their malignancy using a deep learning approach [36]. Each technique has pros and cons, depending on the nature of the investigated molecules.

Microelectromechanical systems (MEMS) based sensors [37,38], fiber Bragg grating (FBG) [39,40], and optical sensors [41] have also played significant roles in identifying breast cancer cells. However, field-effect-transistor (FET) based devices have recently attracted attention in biosensing applications for their many benefits, including small size, low cost, high sensitivity, suitability for CMOS (complementary metal-oxide-semiconductor) technology, controllable electrical response, and reproducibility [42,43]. Tunnel field-effect transistors (TFETs) [44], high-electron-mobility transistors (HEMTs) [45], and fin field-effect transistors (FinFETs) [46] have been used in the past in breast cancer diagnosis. FinFET demonstrates superior performance compared to planar devices and optimizes the short-channel effects (SCEs) by allowing for high scalability, decreased power utilization, and longer battery life [47,48]. The gate-all-around (GAA) design provides enhanced electrostatic control over the channel, higher packing density, a steep subthreshold slope, and high current driving capability [49,50]. During MOS technology downscaling, the gate-stack (GS) design inhibits the increase in off-state leakage current (I_{off}) [51]. Furthermore, the GS design eliminates the mobility degradation and threshold voltage instability that occur with direct deposition of high-k dielectrics on silicon substrates [52,53]. Figure 1 shows a quick comparison of the conventional FinFET and GS-GAA FinFET devices concerning the percentage change in the fundamental DC performance characteristics. It is worth noting that, at a supply voltage of 0.5 V, the GS-GAA FinFET device provides an 86.26% lower off-current (I_{off}), which leads to an improvement of 693.48% in the switching ratio (SR).

Gallium arsenide (GaAs) is considered in the fin area because it has several superior electrical properties to silicon, including high electron mobility and a large energy band gap

Parameters	Conv. FinFET $V_{ds} = 0.05V$	GS-GAA FinFET $V_{ds} = 0.05V$	Conv. FinFET $V_{ds} = 0.5V$	GS-GAA FinFET $V_{ds} = 0.5V$
I_{on} (μA)	2.19	2.32	21.00	22.83
I_{off} (pA)	10.37	1.94	22.78	3.13
SR ($\times 10^6$)	0.21	1.19	0.92	7.30
SS (mV/dec)	67.52	61.49	67.05	61.86
V_{th} (V)	0.27	0.29	0.25	0.27

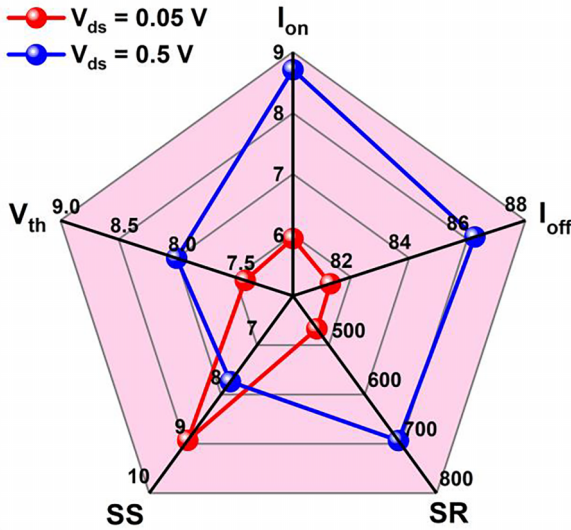

FIG. 1. Conventional FinFET vs GS-GAA FinFET concerning the percentage change in DC performance characteristics.

FIG. 2. Symmetric 3D view of the GaAs-GS-GAA FinFET.

to calculate the switching-ratio-based sensitivity (S_{SR}):

$$S_{SR}(\%) = \left| \frac{SR_{(air)} - SR_{(healthy/cancerous\ cell)}}{SR_{(air)}} \right| \times 100. \quad (1)$$

Further, the healthy and malignant breast cells were taken together in various concentrations, and an investigation was carried out to identify an MDA-MB-231 infection, even in small amounts. When breast cancerous and healthy cells are combined in different concentrations, the effective dielectric constant (ε_{eff}) is determined using the formulas from Brugge-man's model [59,60]:

$$\varepsilon_{eff} = \frac{H_b + \sqrt{H_b^2 + 8\varepsilon_c \varepsilon_h}}{4},$$

with $H_b = (2 - 3C_m)\varepsilon_c - (1 - 3C_m)\varepsilon_h. \quad (2)$

ε_c and ε_h are the dielectric constants of cancerous and healthy cells, and C_m represents the healthy cell fractional volume. Next, the effect of biomolecule occupancy on the device's sensitivity is explored. In biomolecule detection, the cavity area is assumed to have been completely filled. However, during biomolecule immobilization, the target biomolecule only fills a portion of the cavity areas, leaving some empty space, which can change the proposed device's electrical performance for different target biomolecules. Thus, there is a need to consider the biomolecule occupancy factor (γ_{Bio}) as it can potentially affect the sensitivity of the sensor. γ_{Bio} is defined as follows

TABLE I. Values of different parameters used for simulation.

Parameters	Symbol	Value	Unit
Source/drain length	$L_{S/D}$	50	nm
Gate length	L_g	50	nm
Cavity length	C_L	25	nm
Cavity height	C_H	3	nm
Oxide thickness	t_{ox}	3	nm
Fin height	H_{Fin}	30	nm
Fin width	W_{Fin}	15	nm
Gate thickness	G_t	5	nm
Channel doping	N_{Ch}	1×10^{16}	cm^{-3}
Source/drain doping	$N_{S/D}$	5×10^{18}	cm^{-3}
Work function	ϕ_m	4.65	eV
Temperature	T	300	K
Gate-source voltage	V_{gs}	1.5	V
Drain-source voltage	V_{ds}	0.5	V

[54]. The absence of GaAs-based thermodynamically stable, high-quality insulators to augment device standards like SiO$_2$ on silicon is the primary difficulty with GaAs-based devices. Nonetheless, molecular beam epitaxy (MBE) and atomic layer deposition (ALD) have successfully built high-quality dielectrics atop III-V semiconductors [55–57]. Aluminum oxide (Al$_2$O$_3$) is favored as a gate dielectric because of its capacity to stay noncrystalline throughout manufacturing processing, excellent GaAs interface quality, huge 9 eV energy band gap, and high thermal stability [58]. Consequently, we proposed the GaAs-GS-GAA FinFET.

The proposed device employs a GAA design that encloses the gate on all four sides; consequently, four nanocavities are carved beneath the gate electrodes toward the source area for enhanced detection sensitivity. The presence or absence of breast cancer cells affects the dielectric constant of the cavity area. The change in the dielectric constant alters the device's electrical properties, which may then be utilized to identify the presence of sickness in the body. Thus, we used a GaAs-GS-GAA FinFET device in this study to identify breast cancer cells based on their dielectric constant value. MCF-10A and MDA-MB-231 breast cells were chosen for examination and may be produced by the procedure described by Hussein *et al.* [1]. Simulations were run to test the device sensitivity regarding switching ratio by analyzing the drain current characteristics for air (cell free), MCF-10A, and MDA-MB-231 cells. The efficiency of any given sensor is directly proportional to the degree to which it can recognize with a high level of accuracy or precision. Therefore, we utilized Eq. (1)
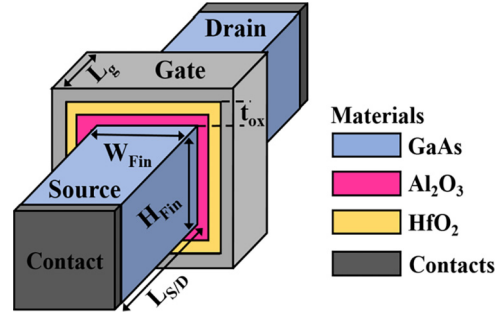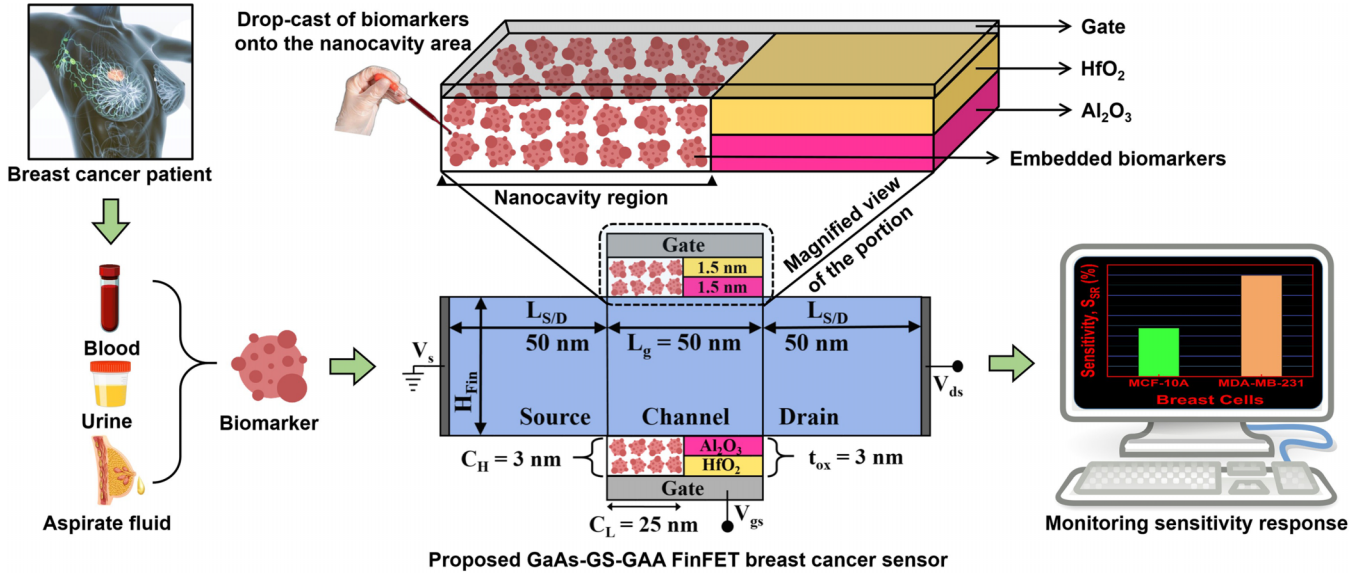
FIG. 3. Diagrammatic representation of the operation of a GaAs-GS-GAA FinFET sensor for breast cancer cell recognition.

[44]:

$$\gamma_{\text{Bio}}(\%) = \frac{\text{Thickness of cavity filled}}{\text{Total thickness of the cavity}} \times 100. \quad (3)$$

The proposed study also investigates how changes to the frequency and device's physical parameters, like fin height, fin width, work function, channel doping, temperature, and drain voltage, influence the device's sensitivity. Based on the findings, optimal device settings for maximizing sensitivity may be selected. Finally, the effectiveness of the proposed breast cancer cell detector is compared to that of already existing breast cancer detectors.

II. DEVICE ARCHITECTURE AND SIMULATION APPROACH

Figure 2 illustrates the symmetric 3D view of the GaAs-GS-GAA FinFET. Table I contains detailed descriptions of the device's structural parameters. The fin area is made of GaAs material. The simulations adhere to the width quantization property by keeping fin width (W_{Fin}) at a constant proportional multiple of fin height (H_{Fin}) [61,62]. In FinFET devices, it is recommended that the W_{Fin} should be less than one-third of the gate length (L_g) and H_{Fin} should be in the $0.6L_g$ to $0.8L_g$ range to minimize the SCEs [63,64]. We considered that recommendation during the device dimension consideration. The gate oxide has a combination of coatings of Al_2O_3 and HfO_2. All sections are uniformly n-type doped with lower channel doping than the source/drain doping to lessen the parasitic capacitance. At 200 MHz frequency, the dielectric constants (k) for MCF-10A and MDA-MB-231 are 4.33 and 24.50, while at 13.6 GHz, they drop to 2.76 and 16.65, respectively [1]. For air, which does not have any cells, k is 1. Figure 3 presents a diagrammatic representation of the operation of a GaAs-GS-GAA FinFET sensor for breast cancer cell recognition. The biomarker was drop-cast onto the nanocavity area carved beneath the gate electrodes to analyze the desired parameters using a technique based on dielectric modulation.

The GaAs-GS-GAA FinFET structure was simulated using the SILVACO-Atlas 3D simulator [65]. The Poisson and continuity equations are frequently used in the device simulation, but additional equations and models are also needed to improve device simulation results. As a result, the simulations include a wide variety of physical models. Quantum confinement effects are an essential design consideration for rapidly scalable devices. To consider the consequences of quantum confinement, the Bohm quantum potential (BQP) model uses a position-dependent quantum potential (Q) with parameters $\gamma = 1.4$ and $\alpha = 0.3$ [66]. Fermi-Dirac statistics, Crowell-Sze impact ionization, concentration-dependent mobility, Klaassen tunneling, Shockley-Read-Hall (SRH) recombination, and band gap narrowing are the other
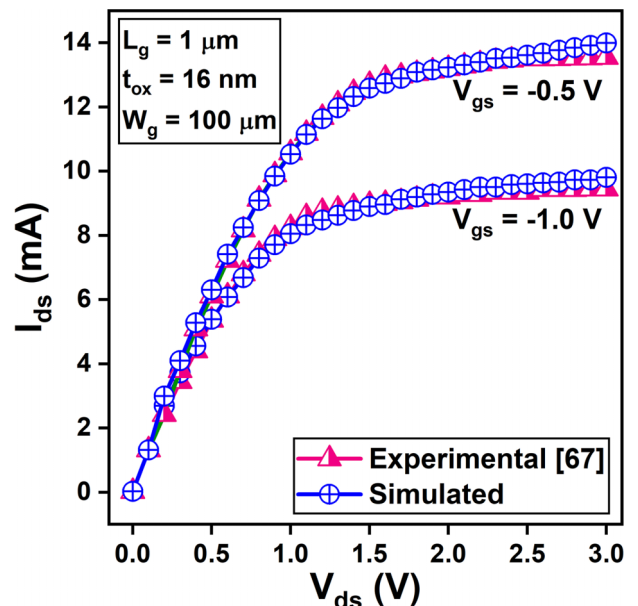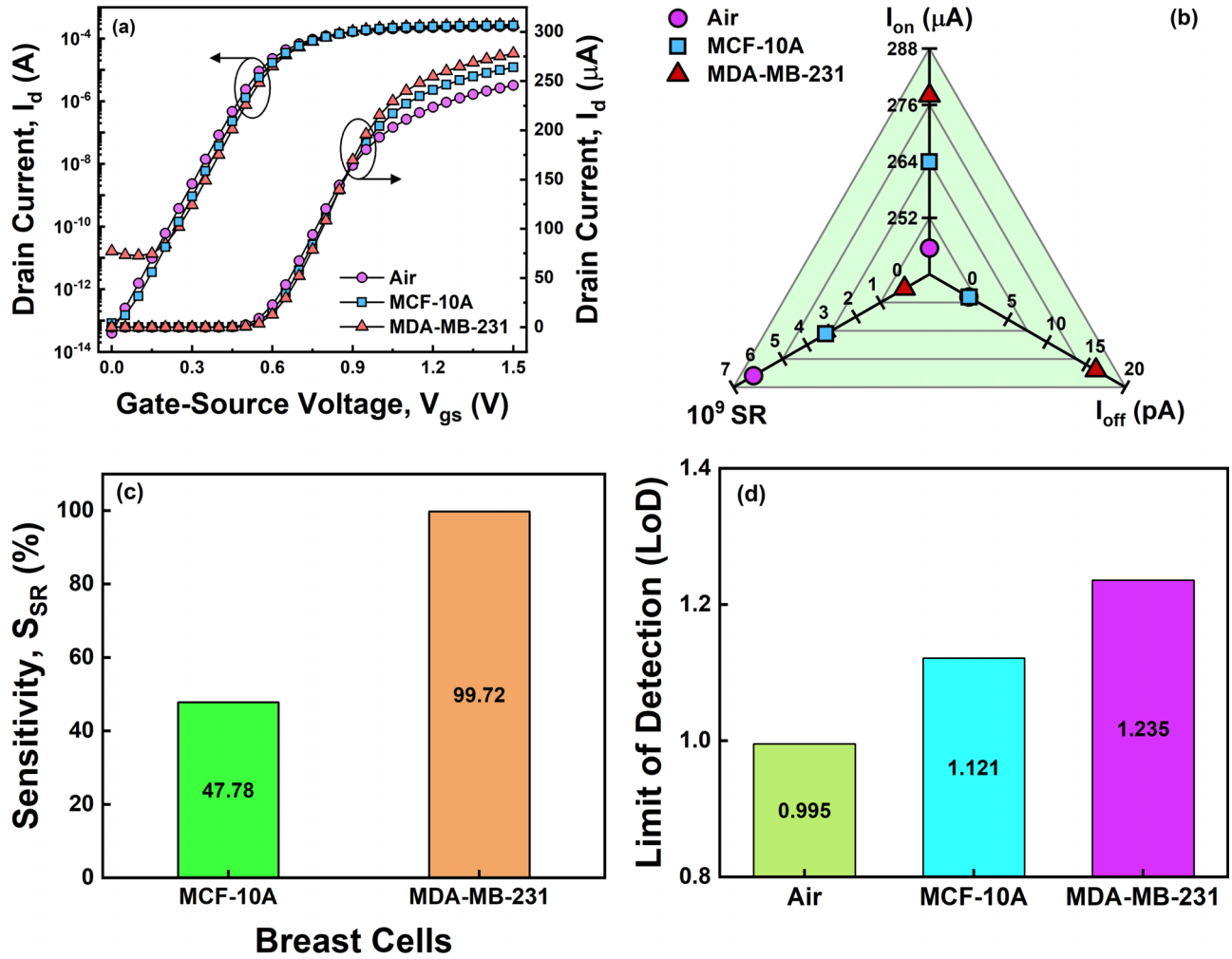

FIG. 4. Calibration curve of an Al_2O_3/GaAs MOSFET.

FIG. 5. (a) Transfer characteristics of the proposed sensor for air, MCF-10A, and MDA-MB-231 in linear and logarithmic form. (b) Fluctuation in I_{on}, I_{off}, and SR for air, MCF-10A, and MDA-MB-231. (c) S_{SR} comparison of MDA-MB-231 and MCF-10A cells. (d) LoD plot for air, MCF-10A, and MDA-MB-231.

standard models that have been incorporated [65]. Additionally, drain current characteristics are simulated using Newton and Block iteration methods for breast cancer cell identification.

We used the findings published by Ye *et al.* [67] to verify the simulation models discussed before. The output characteristics of an Al_2O_3/GaAs MOSFET operated with $V_{gs} = -0.5$ V and $V_{gs} = -1.0$ V are revealed in Fig. 4, along with the experimental and simulated results. The fact that the data sets obtained via simulation and experiment are comparable adds credibility to the simulation models chosen. The steps in creating the proposed GaAs-GS-GAA FinFET device were thoroughly covered in our earlier article [68], including a flowchart illustrating the whole process. Moreover, the cavity region can be created by dry etching the gate dielectric toward the source area.

III. RESULTS AND DISCUSSION

A. Switching-ratio-based sensitivity analysis

Figure 5(a) depicts the transfer characteristics (I_d–V_{gs}) of the proposed sensor for the air, MCF-10A, and MDA-MB-231

in linear and logarithmic forms. The sensor is examined at $V_{ds} = 0.5$ V field bias conditions. The drain current increases with the gate-source voltage (V_{gs}) and attains maximum value for MDA-MB-231. In contrast, the opposite trend is observed in the leakage current and degrades significantly for the MDA-MB-231 cancer cell. Figure 5(b) provides a clearer picture of the fluctuation in on-current (I_{on}), off-current (I_{off}), and switching ratio (SR = I_{on}/I_{off}) (which is subsequently employed as a sensitivity parameter). It can be seen that I_{on} is higher for the MDA-MB-231 cancer cell than for air and healthy cells. It is because introducing the breast cancer cells in the cavity region leads to enhanced effective gate oxide, which in turn increases the coupling between the channel region and gate metal, and thereby on-current. The difference in I_{off} between air and MCF-10A is not very large, but for MDA-MB-231 it is noticeably greater, which brings the SR down to a rather remarkable level. Figure 5(c) compares MDA-MB-231 and MCF-10A cells in terms of their S_{SR}. The graph reveals that the S_{SR} for MDA-MB-231 is 99.72%, and it is 47.78% for MCF-10A. The presence of MDA-MB-231 cells causes a more pronounced shift in I_{off}, which ultimately enhances the device's sensitivity. Figure 5(d) demonstrates the
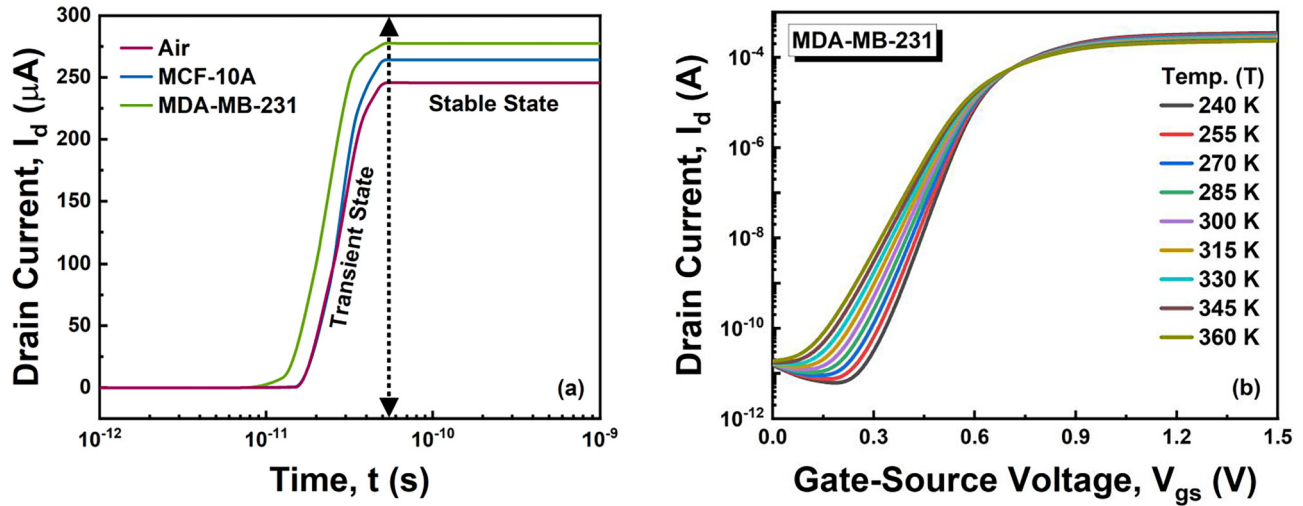
FIG. 6. (a) Transient response of the drain current for air and for MCF-10A and MDA-MB-231 cells. (b) Temperature dependence of the $I_d - V_{gs}$ characteristics of the MDA-MB-231 cancer cell.

limit of detection (LoD) plot for the three samples considered. The lowest concentration of an analyte that can be accurately identified from a sample with a high degree of certainty is known as the LoD [69]. LoD is calculated using the response of slope and standard deviation (SD) of the intercept. The slope and SD of the intercept for MDA-MB-231, MCF-10A, and air are analyzed using the transfer characteristics curve [Fig. 5(a)]. The slope is 0.0002 for all samples, and the SD values come out to be 0.0000749, 0.0000679, and 0.0000603 for MDA-MB-231, MCF-10A, and air. As a result, the LoD obtained for MDA-MB-231 is slightly higher than those for air and MCF-10A. The relevance of reducing execution variability between devices and enhancing sensitivity while designing and producing nano-FET biosensors is provided by these results.

B. Stability and reproducibility analysis

The transient analysis of air and of MCF-10A and MDA-MB-231 cell lines was carried out to test the stability of the proposed sensor. The time it takes for the drain current to settle from its transient state to its steady state is called the settling time (t_{sett}) [70,71]. The transient response is simulated by applying V_{gs} with an amplitude of 1.5 V, a ramp time of 5×10^{-11} s, a stop time of 1×10^{-9} s, and a step time of 1×10^{-12} s. Figure 6(a) shows the transient response of the drain current for air and for MCF-10A and MDA-MB-231 cells. It was observed that the drain current is higher for the MDA-MB-231 cell compared to MCF-10A and air, due to which t_{sett} for the MDA-MB-231 cell is somewhat lower (55.51 ps) than t_{sett} for the MCF-10A cell (60.80 ps) and air (71.58 ps). After t_{sett}, the current becomes steady at a magnitude equal to that at $V_{gs} = 1.5$ V [Fig. 5(a)]. The effect of temperature on the transfer characteristics is investigated to further probe the stability of our proposed sensor. Figure 6(b) displays the temperature dependence of the I_d-V_{gs} characteristics of the MDA-MB-231 cancer cell; it can be observed that the I_d-V_{gs} curves do not vary significantly between 240 and 360 K.

Second, to examine reproducibility, it is necessary to test the sensor's repeatability under controlled use settings. As shown in Fig. 7, we conducted the transient simulation of the proposed sensor for MDA-MB-231 cancerous cells over four cycles with a gap of 30 minutes between each cycle. The drain current is measured for four cycles, and the findings reveal that the drain current can be reliably reproduced with unnoticeable deviation. The above data suggest that the GaAs-GS-GAA FinFET is sufficiently stable and reproducible.

C. Cell viability

The term "oxidative stress" pertains to a state of imbalance between the generation of reactive oxygen species and the capacity of cells to counteract the consequent harm. Cells undergo either apoptotic or necrotic cell death when their antioxidant defense mechanisms are overwhelmed by high amounts of oxidative stress. Zou *et al.* employed a silicon-based attenuated total reflectance terahertz time-domain spectroscopy (ATR THz-TDS) system to monitor cell mortality caused by oxidative stress in MCF-10A breast
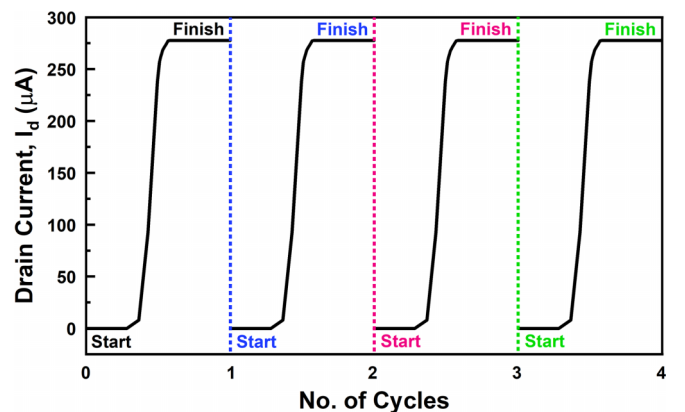

FIG. 7. Transient response of the proposed sensor for MDA-MB-231 cancerous cells over four cycles.
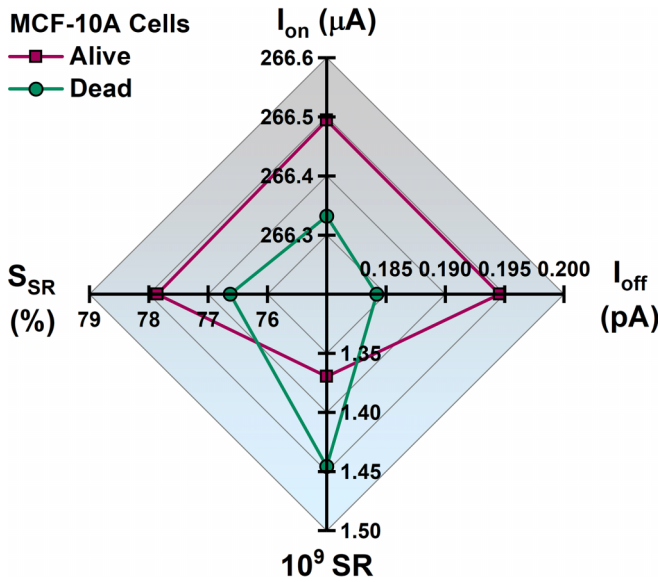
FIG. 8. Variation in I_{on}, I_{off}, SR, and S_{SR} of living and dead MCF-10A breast cells.

cells [72]. This study shows the THz dielectric responses of living and dead MCF-10A breast cells, in which cell death is induced by oxidative stress using a high concentration of hydrogen peroxide (10 mM, H_2O_2). Thus, with the assistance of this study, we have extracted the dielectric constants at 0.3 THz frequency for MCF-10A breast cells before and after the oxidative stress to monitor the electrical response of the proposed sensor on the live and dead cells. The sample under consideration (MCF-10A) may be produced by the procedure described by Zou *et al.* Unfortunately, to the author's best knowledge, no analysis has been performed to characterize the dielectric responses of dead MDA-MB-231 cancerous breast cells. As a result, the electrical response of the proposed sensor on the dead MDA-MB-231 cancerous breast cells could not be determined. The spider-chart depiction of the variation in I_{on}, I_{off}, SR, and S_{SR} of living and dead MCF-10A breast cells is shown in Fig. 8. The induction of cell death through oxidative stress reduces I_{on} from 266.49 to 266.33 μA and I_{off} from 0.195 to 0.184 pA. Since the reduction in I_{off} is bigger than the drop in I_{on}, SR is increased by 5.55%, and S_{SR} is lowered from 77.86% to 76.62%. Despite the relatively minor changes in the electrical response, the sensor under consideration may differentiate between viable and nonviable cells.

D. Early detection

Figures 9(a) and 9(b) demonstrate the transfer characteristics for five different combinations in linear and logarithmic form. In the graph, HC represents the healthy cell and CC is the cancerous cell. The presence of 90% HC and 10% CC indicates a very low quantity of cancerous breast cells, while the presence of 10% HC and 90% CC indicates a very high concentration of breast cancer cells. An enlarged view of the peaks generated by mixing various numbers of healthy and malignant cells is also shown in the insets of Figs. 9(a) and 9(b). It is visible that the drain current and the leakage

current increase with the rise in the concentration of MDA-MB-231 cancerous cells. Figure 9(c) exhibits the spider-chart representation of the variance in I_{on}, I_{off}, and SR over the five different combinations. I_{on} increases from 265 to 277 μA, I_{off} increases by $\sim 10^2$ orders, and SR decreases by 98.48% when the concentration of cancerous cells is raised from 10% to 90%. Thus, the developed sensor can detect the presence of breast cancer cells, even at low concentrations, allowing for early illness diagnosis.

E. Effect of biomolecule occupancy on sensitivity

In order to examine the biomolecule occupancy of the device, five different sites were analyzed: 20%, 40%, 60%, 80%, and 100%. A section of the cavity is covered with biomolecules, while the remaining space is filled with air or left vacant to study the effect of biomolecule occupancy on sensor sensitivity. Figure 10(a) shows the I_{on}, I_{off}, and SR for a healthy MCF-10A cell, while Fig. 10(b) shows the same data for a malignant MDA-MB-231 cell for the five considered occupancy combinations of biomolecules. The increase in the γ_{Bio} leads to an increase in the effective dielectric and capacitance in the cavity area, ultimately increasing I_{on}. For MCF-10A, I_{on} is 256 μA at 20% biomolecule occupancy, which rises to 264 μA for 100% occupancy. Similarly, I_{on} is 267 μA at 20%, which rises to 278 μA at 100% occupancy for MDA-MB-231. I_{off} and SR show the same trend and improve with the increase in γ_{Bio} for MDA-MB-231 and MCF-10A cells. The sensitivity performance for healthy and malignant cells is plotted against different γ_{Bio} in Fig. 10(c). The sensitivity S_{SR} for MDA-MB-231 and MCF-10A decreases slightly with the increase in γ_{Bio}.

F. Effect of device parametric variation on sensitivity

Figures 11(a) to 11(f) collectively demonstrate the S_{SR} of the proposed sensor against the deviation of the mentioned parameters for the MDA-MB-231 cancerous cell. The fin height (H_{Fin}) varies from 30 to 40 nm with a step size of 2.5 nm. The S_{SR} of the proposed device increases with the surge in H_{Fin}, as shown in Fig. 11(a). Fin width (W_{Fin}) is altered from 5 to 15 nm with a step size of 2.5 nm. Figure 11(b) displays the sensitivity S_{SR} as a function of W_{Fin} and shows an improvement in S_{SR} with the rise in W_{Fin}, thus following the path of H_{Fin}. The work function (ϕ_m) is varied from 4.55 to 4.75 eV with an increase of 0.5 eV. The S_{SR} is 85.17% for 4.55 eV, which rises to 99.99% for 4.75 eV, as depicted in Fig. 11(c). Next is channel doping (N_{Ch}), which is considered from 1×10^{16} cm^{-3} to 1×10^{18} cm^{-3}. Figure 11(d) exhibits the variation of S_{SR} with N_{Ch} and shows that the increase in the N_{Ch} results in sensitivity degradation. The temperature (T) range is from 200 to 400 K, with a measurement taken for every 50 K, as portrayed in Fig. 11(e). The reduction in the S_{SR} is marginal from 200 to 300 K, but afterward S_{SR} decreases significantly with the reduction in T. Lastly, in Fig. 11(f), the sensitivity is plotted against the drain voltage (V_{ds}), which varies from 0.1 to 0.5 V with a step size of 0.1 V. The S_{SR} is relatively lower at 0.1 V but increases after that with the increase in V_{ds}, with the highest value being recorded at $V_{ds} = 0.5$ V. Thus, to summarize, the increased levels of
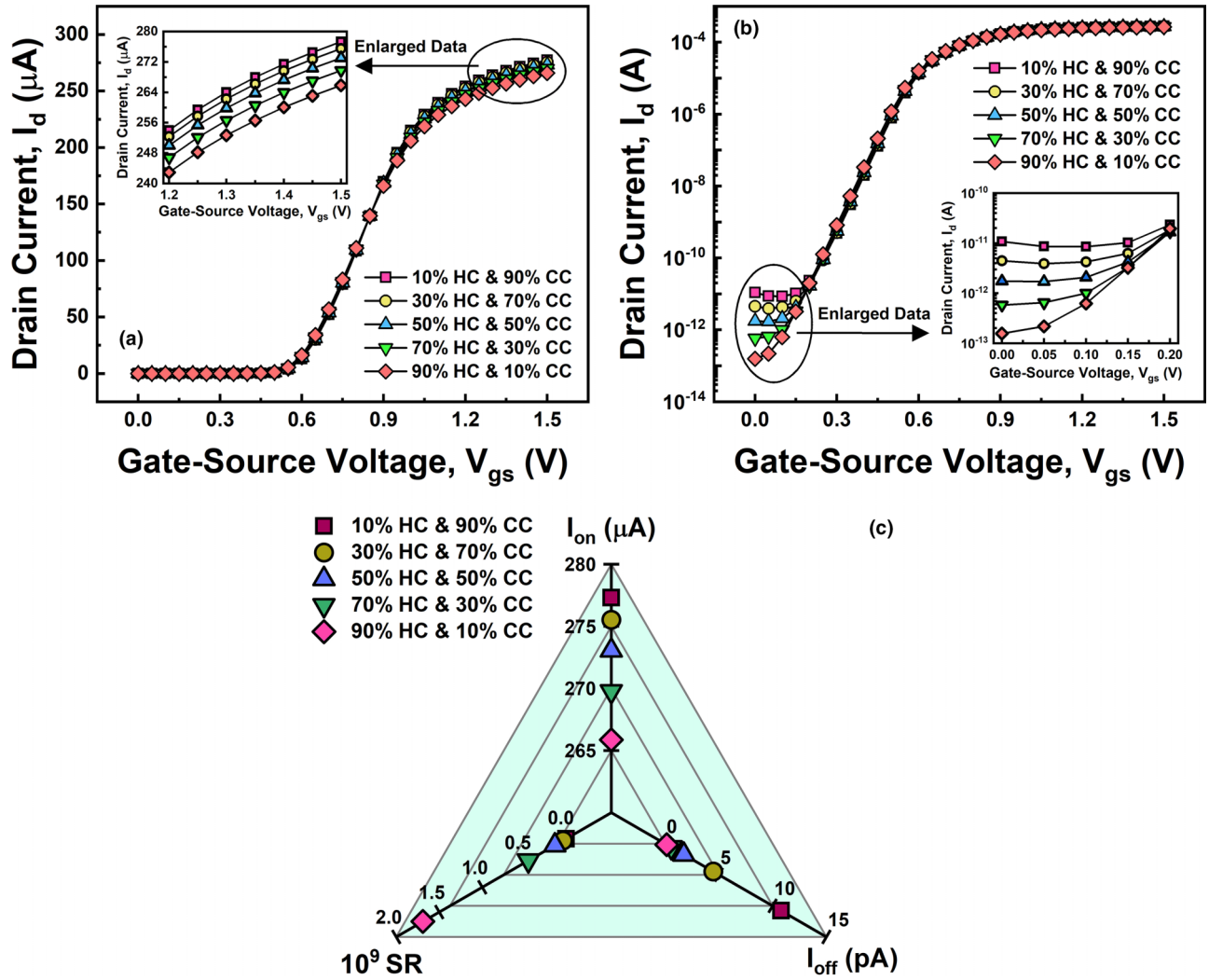
FIG. 9. Transfer characteristics for five different combinations in (a) linear and (b) logarithmic form. (c) Variation in I_{on}, I_{off}, and SR for the combinations considered.

H_{Fin}, W_{Fin}, ϕ_m, and V_{ds}, and the decreased levels of N_{Ch} and T, make it simpler to identify the breast cancer cells.

G. Effect of frequency on sensitivity

We evaluated four parameters, namely I_{on}, I_{off}, SR, and S_{SR} of MDA-MB-231 and MCF-10A breast cells at 13.6 GHz, to study the effect of frequency on these parameters. The comparative statistics for 200 MHz and 13.6 GHz in tabular form are shown in Fig. 12, along with a plot of the percentage change in each performance parameter mentioned above for MDA-MB-231 and MCF-10A breast cells. We evaluated the percentage change considering 200 MHz as the initial value and 13.6 GHz as the final value and plotted the actual percentage change to understand better the impact of the frequency on the respective parameter. When the frequency is raised from 200 MHz to 13.6 GHz, I_{on} decreases by 1.93% and S_{SR} by 2.85%, and I_{off} and SR improve by 3.70% and 2.48%, respectively, for MCF-10A. Similarly, for MDA-MB-231, I_{on} decreases by 0.86% and S_{SR} by 0.69%, and I_{off} and SR improve by 71.57% and 247.06%, respectively, with the rise in

frequency. Thus, the proposed sensor detection sensitivity is significantly better at 200 MHz compared to 13.6 GHz for MDA-MB-231 and MCF-10A.

H. Comparison with published breast cancer detectors

An evaluation of the proposed breast cancer sensor against existing breast cancer detectors is required to determine its efficacy. Table II gives an overview of the proposed Fin-FET breast cancer sensor with other already published breast cancer sensors regarding the change in drain current (ΔI_{ds}) and drain current sensitivity (S_{Id}). The ΔI_{ds} data were unavailable for the reduced graphene oxide (rGO) encapsulated nanoparticle (NP) based FET biosensor, so we mentioned the device's sensitivity, which is about 3.9%. The highest reported ΔI_{ds} was 6 μA for the AlGaN/GaN HEMT structure, with ΔI_{ds} for the remaining devices being relatively low. The proposed GaAs-GS-GAA FinFET sensor exhibits improved results compared to the breast cancer detectors mentioned in Table II, with ΔI_{ds} of about 32.5 μA and S_{Id} of 13.21%.
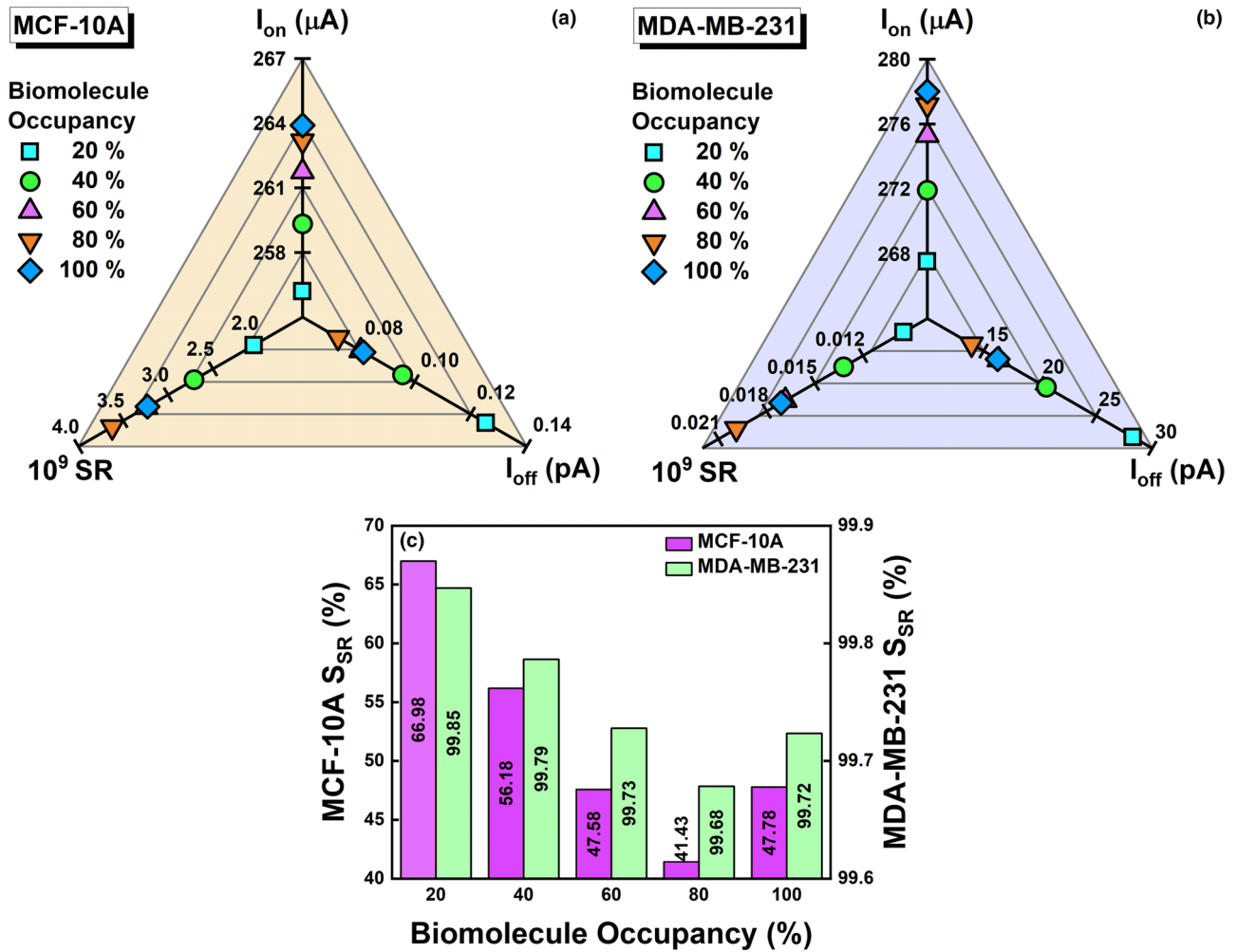
FIG. 10. Biomolecule occupancy impact on I_{on}, I_{off}, and SR for (a) MCF-10A and (b) MDA-MB-231. (c) Sensitivity performance for healthy and malignant cells against different γ_{Bio}.

IV. CONCLUSION

The current work details the usage of a GaAs-GS-GAA FinFET to monitor the device switching ratio to achieve the electrical identification of the MDA-MB-231 breast cancer cell. In order to increase the detection sensitivity, the suggested sensor makes use of four nanocavities that are carved underneath the gate electrodes. To emphasize the advantages of GS-GAA FinFET over traditional FinFET, a percentage change in the crucial electrical parameters is displayed for both types of FinFET. The switching-ratio-based sensitivity of the sensor is measured for healthy and malignant breast cells and turns out to be 47.78% and 99.72%, respectively. The sensor was evaluated for its reproducibility and stability

TABLE II. Overview of proposed FinFET-engineered cancer detector vs other published cancer detectors.

| References	Year	Platform device	Detection	Change in drain current, ΔI_{ds} (μA)	Drain current sensitivity, $S_{Id}(\%)$
[45]	2009	AlGaN/GaN HEMT	c-erbB-2, a breast cancer marker	6	–
[73]	2011	rGO encapsulated NP-based FET	HER2 and EGFR, a breast cancer marker	–	3.9
[74]	2020	Apta-cyto-sensor	MDA-MB-231 breast cancer cells	3	–
[75]	2021	CNT FET biosensor	Breast cancer exosomal miRNA21	1.65	–
[44]	2022	DL-NC-FE-TFET	T47D, Hs578T, MDA-MB-231, and MCF-7 breast cancer lines	1.83	–
This work		GaAs-GS-GAA FinFET	MDA-MB-231 breast cancer cells	32.5	13.21
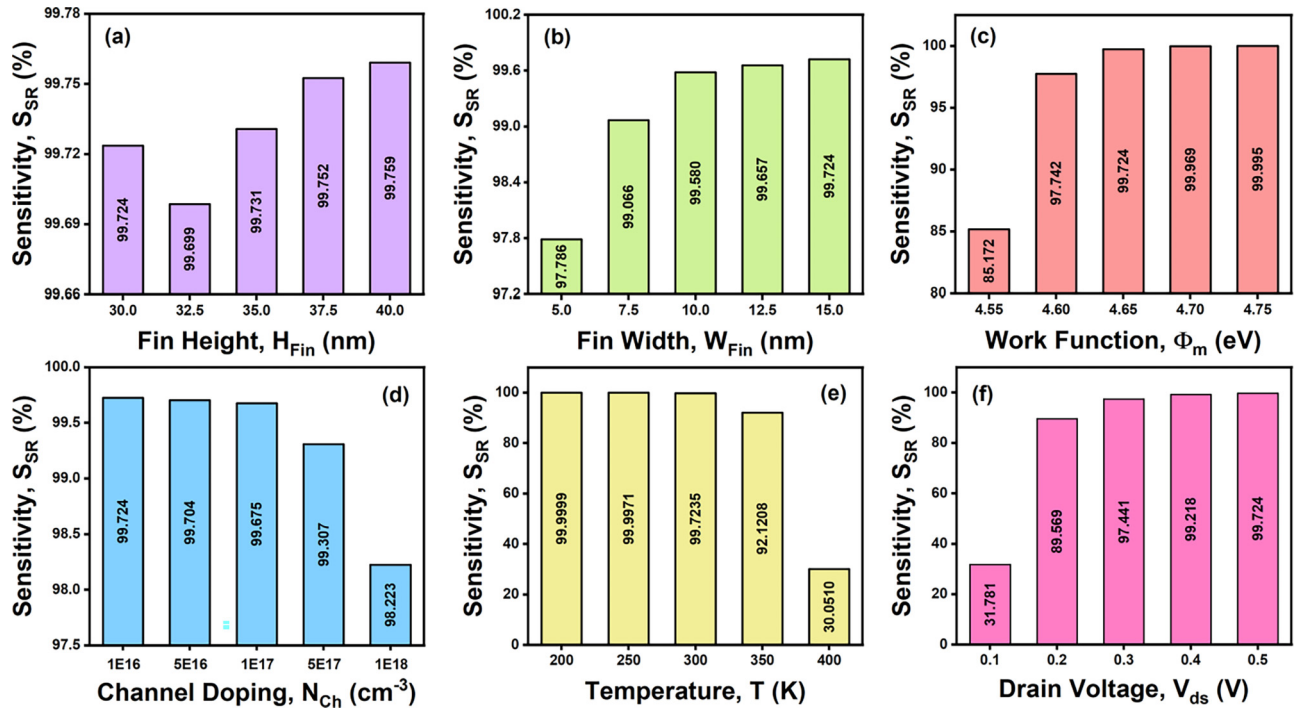
FIG. 11. S_{SR} of the proposed sensor against the deviation of mentioned parameters for the MDA-MB-231 cancerous cell.

and was found to be repeatable and adequately stable with settling times of 55.51 ps for the MDA-MB-231 cell, 60.80 ps for the MCF-10A cell, and 71.58 ps for air. Furthermore, the sensor is capable of distinguishing between viable and nonviable cells based on changes in their electrical response. The research also shows that breast cancer cells can be identified with the assistance of Bruggeman's model even when

present in a mixed solution of malignant and healthy cells, even though the quantity of cancerous cells is lower. The effect of biomolecule occupancy and frequency fluctuations on the device's sensitivity is also investigated. This research also describes how to enhance the sensing performance by altering the fin height, fin width, work function, channel doping, temperature, and drain voltage. The proposed sensor can better identify malignant cells when the levels of H_{Fin}, W_{Fin}, ϕ_m, and V_{ds} increase and the N_{Ch} and T levels decrease. Finally, this work compared the suggested GaAs-GS-GAA FinFET sensor to previously published breast cancer sensors regarding the change in drain current and drain current sensitivity and found that the proposed sensor performed much better. Thus, the proposed GaAs-GS-GAA FinFET sensor may be considered an intriguing candidate for MDA-MB-231 breast cancer cell detection.

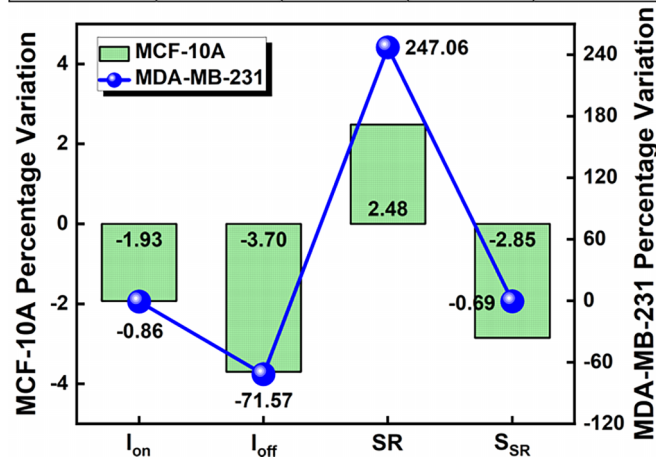| Parameters	MCF-10A		MDA-MB-231	
	200 MHz	13.6 GHz	200 MHz	13.6 GHz
I_{on} (μA)	263.90	258.80	278.00	275.60
I_{off} (pA)	0.081	0.078	16.25	4.62
SR ($\times 10^9$)	3.23	3.31	0.017	0.059
S_{SR} (%)	47.78	46.42	99.72	99.03

FIG. 12. Percentage change in each mentioned performance parameter for MDA-MB-231 and MCF-10A breast cells.

[1] M. Hussein, F. Awwad, D. Jithin, H. El Hasasna, K. Athamneh, and R. Iratni, Breast cancer cells exhibits specific dielectric signature *in vitro* using the open-ended coaxial probe technique from 200 MHz to 13.6 GHz, Sci. Rep. **9**, 4681 (2019).

[2] World Health Organization, Cancer, accessed Feb. 03, 2022, https://www.who.int/news-room/fact-sheets/detail/cancer.

[3] Early Breast Cancer Trialists' Collaborative Group, Effects of chemotherapy and hormonal therapy for early breast cancer on recurrence and 15-year survival: An overview of the randomized trials, Lancet **365**, 1687 (2005).

[4] Cancer Research UK, Breast Cancer Incidence (Invasive) Statistics, 2015 (unpublished).

[5] T. Gerecsei, I. Erdődi, B. Peter, C. Hős, S. Kurunczi, I. Derényi, B. Szabó, and R. Horvath, Adhesion force measurements on functionalized microbeads: An in-depth comparison of computer controlled micropipette and fluidic force microscopy, J. Colloid Interface Sci. **555**, 245 (2019).

[6] R. P. Rand and A. C. Burton, Mechanical properties of the red cell membrane: I. Membrane stiffness and intracellular pressure, Biophys. J. **4**, 115 (1964).

[7] F. Guilak, W. R. Jones, H. P. Ting-Beall, and G. M. Lee, The deformation behavior and mechanical properties of chondrocytes in articular cartilage, Osteoarthr. Cartil. **7**, 59 (1999).

[8] M. Schmidt, M. K. Hourfar, S.-B. Nicol, H.-P. Spengler, T. Montag, and E. Seifried, FACS technology used in a new rapid bacterial detection method, Transfus. Med. **16**, 355 (2006).

[9] I. Antoniadi, V. Skalický, G. Sun, W. Ma, D. W. Galbraith, O. Novák, and K. Ljung, Fluorescence activated cell sorting-A selective tool for plant cell isolation and analysis, Cytom. Part A **101**, 725 (2022).

[10] X. Liao, M. Makris, and X. M. Luo, Fluorescence-activated cell sorting for purification of plasmacytoid dendritic cells from the mouse bone marrow, J. Vis. Exp. **117**, 54641 (2016).

[11] D. L. Adams, P. Zhu, O. V. Makarova, S. S. Martin, M. Charpentier, S. Chumsri, S. Li, P. Amstutz, and C. M. Tang, The systematic study of circulating tumor cell isolation using lithographic microfilters, RSC Adv., **4**, 4334 (2014).

[12] P. Li, Z. Mao, Z. Peng, L. Zhou, Y. Chen, P. H. Huang, C. I. Truica, J. J. Drabick, W. S. El-Deiry, M. Dao, S. Suresh, and T. J. Huang, Acoustic separation of circulating tumor cells, Proc. Natl. Acad. Sci. USA **112**, 4970 (2015).

[13] H. Song, J. M. Rosano, Y. Wang, C. J. Garson, B. Prabhakarpandian, and K. Pant, Continuous-flow sorting of stem cells and differentiation products based on dielectrophoresis, Lab Chip **15**, 1320 (2015).

[14] Y. Zhou, Y. Wang, and Q. Lin, A microfluidic device for continuous-flow magnetically controlled capture and isolation of microparticles, J. Microelectromech. Syst. **19**, 743 (2010).

[15] B. Aguilar-Bravo and P. Sancho-Bru, Laser capture microdissection: Techniques and applications in liver diseases, Hepatol. Int. **13**, 138 (2019).

[16] J. A. Herrera, V. Mallikarjun, S. Rosini, M. A. Montero, C. Lawless, S. Warwood, R. O'Cualain, D. Knight, M. A. Schwartz, and J. Swift, Laser capture microdissection coupled mass spectrometry (LCM-MS) for spatially resolved analysis of formalin-fixed and stained human lung tissues, Clin. Proteomics **17**, 24 (2020).

[17] J. G. Elmore, M. B. Barton, V. M. Moceri, S. Polk, P. J. Arena, and S. W. Fletcher, Ten-year risk of false positive screening mammograms and clinical breast examinations, New England J. Med. **338**, 1089 (1998).

[18] Cancer Facts and Figures. [Online] American Cancer Society. (2007), available: https://www.cancer.org.

[19] P. Skaane, S. Hofvind, and A. Skjennald, Randomized trial of screen-film versus full-field digital mammography with soft-copy reading in population-based screening program: Follow-up and final results of Oslo II study, Radiology **244**, 708 (2007).

[20] J.-L. Gonzalez-Hernandez, A. N. Recinella, S. G. Kandlikar, D. Dabydeen, L. Medeiros, and P. Phatak, Technology, application and potential of dynamic breast thermography for the detection of breast cancer, Int. J. Heat Mass Transf. **131**, 558 (2019).

[21] S. J. Lord, W. Lei, P. Craft, J. N. Cawson, I. Morris, S. Walleser, A. Griffiths, S. Parker, and N. Houssami, A systematic review of the effectiveness of magnetic resonance imaging (MRI) as an addition to mammography and ultrasound in screening young women at high risk of breast cancer, Eur. J. Cancer **43**, 1905 (2007).

[22] M. Säbel and H. Aichinger, Recent developments in breast imaging, Phys. Med. Biol. **41**, 315 (1996).

[23] E. C. Fear and M. A. Stuchly, Microwave detection of breast cancer, IEEE Trans. Microw. Theory Techn. **48**, 1854 (2000).

[24] S. C. Hagness, A. Taflove, and J. E. Bridges, Three-dimensional FDTD analysis of a pulsed microwave confocal system for breast cancer detection: Design of an antenna-array element, IEEE Trans. Antennas Propag. **47**, 783 (1999).

[25] X. Li, E. J. Bond, B. D. V. Veen, and S. C. Hagness, An overview of ultra-wideband microwave imaging via space-time beam-forming for early-stage breast-cancer detection, IEEE Antennas Propag. Mag. **47**, 19 (2005).

[26] S. Kwon and S. Lee, Recent advances in microwave imaging for breast cancer detection, Int. J. Biomed. Imag. **2016**, 5054912 (2016).

[27] T. Kim, J. Oh, B. Kim, J. Lee, S. Jeon, and J. Pack, A study of dielectric properties of fatty, malignant and fibro-glandular tissues in female human breast, in *Proceedings of the Asia-Pacific and 19th International Zurich Symposium on Electromagnetic Compatability, Singapore, 2008* (IEEE, Piscataway, NJ, 2008), pp. 216–219.

[28] W. T. Joines, Y. Zhang, C. Li, and R. L. Jirtle, The measured electrical properties of normal and malignant human tissues from 50 to 900 MHz, Med. Phys. **21**, 547 (1994).

[29] L. Chin and M. Sherar, Changes in dielectric properties of *ex vivo* bovine liver at 915 MHz during heating, Phys. Med. Biol. **46**, 197 (2001).

[30] U. Andergassen, M. Zebisch, A. C. Kölbl, A. König, S. Heublein, L. Schröder, S. Hutter, K. Friese, and U. Jeschke, Real-time qPCR-based detection of circulating tumor cells from blood samples of adjuvant breast cancer patients: A preliminary study, Breast Care **11**, 194 (2016).

[31] T. Y. Ryu, K. Kim, S.-K. Kim, J.-H. Oh, J.-K. Min, C.-R. Jung, M.-Y. Son, D.-S. Kim, and H.-S. Cho, SETDB1 regulates SMAD7 expression for breast cancer metastasis, BMB Rep. **52**, 139 (2019).

[32] S. Wang, X. Chen, H. Luan, D. Gao, S. Lin, Z. Cai, J. Liu, H. Liu, and Y. Jiang, Matrix-assisted laser desorption/ionization mass spectrometry imaging of cell cultures for the lipidomic analysis of potential lipid markers in human breast cancer invasion, Rapid Commun. Mass Spectrom. **30**, 533 (2016).

[33] L. C. Whelan, K. A. R. Power, D. T. McDowell, J. Kennedy, and W. M. Gallagher, Applications of SELDI-MS technology in oncology, J. Cell. Mol. Med. **12**, 1535 (2008).

[34] R. Eghlimi, X. Shi, J. Hrovat, B. Xi, and H. Gu, Triple negative breast cancer detection using LC-MS/MS lipidomic profiling, J. Proteome Res. **19**, 2367 (2020).

[35] N. Kanyo, K. D. Kovács, S. V. Kovács, B. Béres, B. Peter, I. Székács, and R. Horvath, Single-cell adhesivity distribution of glycocalyx digested cancer cells from high spatial resolution label-free biosensor measurements, Matrix Biol. Plus **14**, 100103 (2022).

[36] V. K. Lam, T. C. Nguyen, B. M. Chung, G. Nehmetallah, and C. B. Raub, Quantitative assessment of cancer cell morphology and motility using telecentric digital holographic microscopy and machine learning, Cytom. Part A **93**, 334 (2018).

[37] H. J. Pandya, K. Park, and J. P. Desai, Design and fabrication of a flexible MEMS-based electro-mechanical sensor array for breast cancer diagnosis, J. Micromech. Microeng. **25**, 075025 (2015).

[38] K. Park, W. Chen, M. A. Chekmareva, D. J. Foran, and J. P. Desai, Electromechanical coupling factor of breast tissue as a biomarker for breast cancer, IEEE Trans. Biomed. Eng. **65**, 96 (2018).

[39] N. Ayyanar, G. T. Raja, M. Sharma, and D. S. Kumar, Photonic crystal fiber-based refractive index sensor for early detection of cancer, IEEE Sensors J. **18**, 7093 (2018).

[40] D. Sun, Y. Ran, and G. Wang, Label-free detection of cancer biomarkers using an in-line taper fiber-optic interferometer and a fiber Bragg grating, Sensors **17**, 2559 (2017).

[41] M. A. Ahmad, A. Najar, A. E. Moutaouakil, N. Nasir, M. Hussein, S. Raji, and A. H. Alnaqbi, Label-free cancer cells detection using optical sensors, IEEE Access **6**, 55807 (2018).

[42] M. Verma, S. Tirkey, S. Yadav, D. Sharma, and D. S. Yadav, Performance assessment of a novel vertical dielectrically modulated TFET based biosensor, IEEE Trans. Electron Devices **64**, 3841 (2017).

[43] A. Chhabra, A. Kumar, and R. Chaujar, Sub-20 nm GaAs junctionless FinFET for biosensing application, Vacuum **160**, 467 (2019).

[44] S. Singh and S. Singh, Dopingless negative capacitance ferroelectric TFET for breast cancer cells detection: Design and sensitivity analysis, IEEE Trans. Ultrason. Ferroelectr. Freq. Control **69**, 1120 (2022).

[45] K. H. Chen, B. S. Kang, H. T. Wang, T. P. Lele, F. Ren, Y. L. Wang, C. Y. Chang, S. J. Pearton, D. M. Dennis, J. W. Johnson, P. Rajagopal, J. C. Roberts, E. L. Piner, and K. J. Linthicum, c-erbB-2 sensing using AlGaN/GaN high electron mobility transistors for breast cancer detection, Appl. Phys. Lett. **92**, 192103 (2009).

[46] R. Ramesh, M. Madheswaran, and K. Kannan, Nanoscale Fin-FET sensor for determining the breast cancer tissues using wavelet coefficients, J. Mech. Med. Biol. **11**, 1295 (2011).

[47] V. B. Sreenivasulu and V. Narendar, Junctionless SOI FinFET with advanced spacer techniques for sub-3 nm technology nodes, AEU Int. J. Electron. Commun. **145**, 154069 (2022).

[48] B. Kumar and R. Chaujar, Numerical study of JAM-GS-GAA FinFET: A fin aspect ratio optimization for upgraded analog and intermodulation distortion performance, Silicon **14**, 309 (2022).

[49] Y. C. Huang, M. H. Chiang, S. J. Wang, and J. G. Fossum, GAAFET versus pragmatic FinFET at the 5nm Si-based CMOS technology node, IEEE J. Electron Devices Soc. **5**, 164 (2017).

[50] B. Kumar and R. Chaujar, Analog and RF performance evaluation of junctionless accumulation mode (JAM) gate stack gate all around (GS-GAA) FinFET, Silicon **13**, 919 (2021).

[51] N. Gupta and R. Chaujar, Optimization of high-k and gate metal work function for improved analog and intermodulation performance of gate stack (GS)-GEWE-SiNW MOSFET, Superlattices Microstruct. **97**, 630 (2016).

[52] A. Kerber, E. Cartier, L. Pantisano, R. Degraeve, T. Kauerauf, Y. Kim, A. Hou, G. Groeseneken, and H. E. Maes, Origin of the threshold voltage instability in SiO_2/HfO_2 dual layer gate dielectrics, IEEE Electron Device Lett., **24**, 87 (2003).

[53] K. Onishi, C. S. Kang, R. Choi, H. J. Cho, S. Gopalan, R. E. Nieh, S. A. Krishnan, and J. C. Lee, Improvement of surface carrier mobility of HfO_2 MOSFETs by high-temperature forming gas annealing, IEEE Trans. Electron Devices **50**, 384 (2003).

[54] S.-H. Chen, W.-S. Liao, H.-C. Yang, S.-J. Wang, Y.-G. Liaw, H. Wang, H. Gu, and M.-C. Wang, High-performance III-V MOS-FET with nano-stacked high-*k* gate dielectric and 3D fin-shaped structure, Nanoscale Res. Lett. **7**, 431 (2012).

[55] B. Yang, P. D. Ye, J. Kwo, M. R. Frei, H.-J. L. Gossmann, J. P. Mannaerts, M. Sergent, M. Hong, K. Ng, and J. Bude, Impact of metal/oxide interface on DC and RF performance of depletion-mode GaAs MOSFET employing MBE grown $Ga_2O_3(Gd_2O_3)$ as gate dielectric, J. Cryst. Growth **251**, 837 (2003).

[56] C. P. Chen, Y. J. Lee, Y. C. Chang, Z. K. Yang, M. Honga, J. Kwo, H. Y. Lee, and T. S. Lay, Structural and electrical characteristics of $Ga_2O_3 (Gd_2O_3)$ GaAs under high temperature annealing, J. Appl. Phys. **100**, 104502 (2006).

[57] P. D. Ye, G. D. Wilk, B. Yang, J. Kwo, S. N. G. Chu, S. Nakahara, H.-J. L. Gossmann, J. P. Mannaerts, M. Hong, K. K. Ng, and J. Bude, GaAs metal-oxide-semiconductor field-effect transistor with nanometer-thin dielectric grown by atomic layer deposition, Appl. Phys. Lett. **83**, 180 (2003).

[58] H. C. Lin, P. D. Ye, and G. D. Wilk, Leakage current and breakdown electric-field studies on ultrathin atomic-layer-deposited Al_2O_3 on GaAs, Appl. Phys. Lett. **87**, 182904 (2005).

[59] G. A. Niklasson, C. G. Granqvist, and O. Hunderi, Effective medium models for the optical properties of inhomogeneous materials, Appl. Opt. **20**, 26 (1981).

[60] Wikipedia, Effective Medium Approximations, accessed Jan. 27, 2023, https://en.wikipedia.org/wiki/Effective_medium_approximations.

[61] A. Razavieh, P. Zeitzoff, and E. J. Nowak, Challenges and limitations of CMOS scaling for FinFET and beyond architectures, IEEE Trans. Nanotechnol. **18**, 999 (2019).

[62] B. Kumar, M. Sharma, and R. Chaujar, Gate electrode work function engineered JAM-GS-GAA FinFET for analog/RF applications: Performance estimation and optimization, Microelectronics J., **135**, 105766 (2023).

[63] Y. Omura, H. Konishi, and K. Yoshimoto, Impact of fin aspect ratio on short-channel control and drivability of multiple-gate SOI MOSFET's, J. Semicond. Tech. Sci. **8**, 302 (2008).

[64] S. K. Mohapatra, K. P. Pradhan, D. Singh, and P. K. Sahu, The role of geometry parameters and fin aspect ratio of sub-20 nm SOI FinFET: An analysis towards analog and RF circuit design, IEEE Trans. Nanotechnol. **14**, 546 (2015).

[65] *ATLAS User's Manual* (SILVACO International, Santa Clara, CA, 2016).

[66] B. Kumar and R. Chaujar, TCAD temperature analysis of Gate Stack Gate All Around (GS-GAA) FinFET for improved RF and wireless performance, Silicon **13**, 3741 (2021).

[67] P. D. Ye, G. D. Wilk, J. Kwo, B. Yang, H.-J. L. Gossmann, M. Frei, S. N. G. Chu, J. P. Mannaerts, M. Sergent, M. Hong, K. K. Ng, and J. Bude, GaAs MOSFET with oxide gate dielectric grown by atomic layer deposition, IEEE Electron Device Lett. **24**, 209 (2003).

[68] B. Kumar and R. Chaujar, Numerical simulation of analog metrics and parasitic capacitances of GaAs GS-GAA FinFET for ULSI switching applications, Eur. Phys. J. Plus **137**, 110 (2022).

[69] D. Martens and P. Bienstman, Study on the limit of detection in MZI-based biosensor systems, Sci. Rep. **9**, 5767 (2019).

[70] A. Wei, M. J. Sherony, and D. A. Antoniadis, Transient behavior of the kink effect in partially-depleted SOI MOSFET's, IEEE Electron Device Lett. **16**, 494 (1995).

[71] P. Dwivedi, R. Singh, B. S. Sengar, A. Kumar, and V. Garg, A new simulation approach of transient response to enhance the selectivity and sensitivity in tunneling field effect transistor-based biosensor, IEEE Sens. J. **21**, 3201 (2021).

[72] Y. Zou, Q. Liu, X. Yang, H.-C. Huang, J. Li, L.-H. Du, Z.-R. Li, J.-H. Zhao, and L.-G. Zhu, Label-free monitoring of cell death induced by oxidative stress in living human cells using terahertz ATR spectroscopy, Biomed. Opt. Express **9**, 14 (2018).

[73] S. Myung, A. Solanki, C. Kim, J. Park, K. S. Kim, and K.-B. Lee, Graphene-encapsulated nanoparticle-based biosensor for the selective detection of cancer biomarkers, Adv. Mater. **23**, 2221 (2011).

[74] S. Akhtartavan, M. Karimi, N. Sattarahmady, and H. Heli, An electrochemical signal-on apta-cyto-sensor for quantitation of circulating human MDA-MB-231 breast cancer cells by transduction of electro-deposited non-spherical nanoparticles of gold, J. Pharmaceutical Biomed. Anal. **178**, 112948 (2020).

[75] T. Li, Y. Liang, J. Li, Y. Yu, M.-M. Xiao, W. Ni, Z. Zhang, and G.-J. Zhang, Carbon nanotube field-effect transistor biosensor for ultrasensitive and label-free detection of breast cancer exosomal miRNA21, Anal. Chem. **93**, 15501 (2021).